Science of the Total Environment 891 (2023) 164545

Contents lists available at ScienceDirect

Science of the Total Environment

journal homepage: www.elsevier.com/locate/scitotenv

Combined use of UAV-SfM surveys, soil particle tracking with RFID tags and a sediment connectivity index to study plot-scale sediment transport

Manuel López-Vicente [a], Seigo Fujiwara [b], Yuichi Onda [c,*], Shohei Kozuka [d], Yoshifumi Wakiyama [e], Hiroaki Kato [c]

[a] Group Aquaterra, Interdisciplinary Centre of Chemistry and Biology, Universidade da Coruña (CICA-UDC), A Coruña 15071, Spain
[b] Degree Programs in Life and Earth Sciences, University of Tsukuba, Tsukuba city, Japan
[c] Center for Research in Isotopes and Environmental Dynamics, University of Tsukuba, Tsukuba city, Japan
[d] Ministry of Environment, 1-2-2 Kasumigaseki, Chiyoda-ku, Tokyo, Japan
[e] Institute of Environmental Radioactivity, Fukushima University, Fukushima City, Japan

HIGHLIGHTS

- Low-flying (5–10 m) UAV-SfM survey was compared with terrestrial laser scanner.
- The standard deviation of differences between UAV-SfM and TLS methods was 3.3 mm.
- RFID tags were located with an orthomosaic generated by UAV-SfM method.
- The RMSE value of the RFID tags locating accuracy was of 3.1 cm.
- Combined use of UAV-SfM and RFID tags give new insights on erosion at plot scale.

GRAPHICAL ABSTRACT

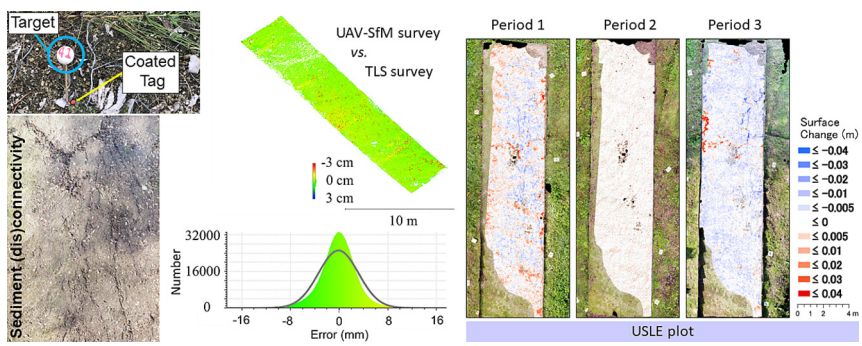

ARTICLE INFO

Editor: Ouyang Wei

Keywords:
RFID
UAV-SfM
Particle tracking
Soil erosion
TLS
Sediment connectivity

ABSTRACT

To explore the processes of soil erosion at the plot scale, Digital surface model of Differences (DoD) maps (Unmanned Aerial Vehicle – Structure from Motion (UAV-SfM) method) and data from Radio Frequency Identification (RFID) tags were analysed. The comparison of differences in accuracy of UAV-SfM and 3D terrestrial laser scanner (TLS) measurements, and the integration of the UAV-SfM method and soil particle tracing with RFID tag locations were conducted to assess sediment transport in a plot in Fukushima prefecture, Japan. The Universal Soil Loss Equation (USLE) plot was installed and kept with no vegetation and no cultivation. Water and sediment discharges were measured at the outlet of the plot, and the topographic index of runoff and sediment connectivity (IC) –focused on surface roughness– was also estimated. Based on field surveys, four periods were defined. Locations of RFID tags were firstly determined by using orthoimages derived from the UAV-SfM method and then compared with those locations measured with a laser total station. The mean and standard deviation of difference amounts of UAV-SfM were of 1 and 3.3 mm, respectively. On average, the RFID tags were located with an accuracy of 3.1 cm (RMSE). Although data of tags tracing showed short transport distances with rill erosion, the results of the UAV-SfM surveys showed an increase of sediment connectivity (SC) over the study period that may explain the largest sediment discharge, especially of fine soil particles. The concurrence of higher values of SC as well as the development of new and longer rills demonstrated the important activity of net soil loss in our study site. The combination of distinct methods and techniques, all providing accurate measurements, shed light on the sediment transport process at short distances, which affects the net water and sediment discharge at larger scales.

* Corresponding author.
E-mail addresses: manuel.lopez.vicente@udc.es (M. López-Vicente), onda@geoenv.tsukuba.ac.jp y-onda@jc5.so-net.ne.jp (Y. Onda).

http://dx.doi.org/10.1016/j.scitotenv.2023.164545
Received 4 February 2023; Received in revised form 27 May 2023; Accepted 27 May 2023
Available online 30 May 2023
0048-9697/© 2023 Elsevier B.V. All rights reserved.

1. Introduction

Soil erosion is one of the factors degrading landscapes and cropland, causing undesired in situ (e.g. less topsoil fertility, organic carbon content, and water storage capacity) and off-site (e.g. water bodies eutrophication, reservoir siltation, decrease in groundwater recharge) consequences (Ritchie, 2000). Soil erosion fosters soil degradation, which is defined by the FAO (Food and Agriculture Organization of the United Nations) as a change in the soil health status resulting in a diminished capacity to provide goods and services for its beneficiaries. Recently, Sartori et al. (2019) estimated in $8 billion the annual global costs of soil erosion to gross domestic product. Soil erosion includes the processes of soil particle detachment and transportation by erosive agents (Ellison, 1947). The detachment by raindrop impact (splash) is the first stage in the soil erosion process. The subsequent transport of detached soil particles by sheet flow causes interrill erosion, and the detachment and transport by concentrated flow causes rill erosion (Cerdan et al., 2006). In spite of the short distance travelled by soil particles due to splash erosion, the quantification of the total loss of soil due to the impact of raindrops is difficult (Fernández-Raga et al., 2017). These authors stressed the need of better know the basic factors that influence splash erosion. Although the features produced by rill erosion are easy to distinguish on the ground, interrill water erosion is one of the main types of soil loss (Gilley, 2005). Many land uses related to human activities, such as paddy fields, farmlands and urban areas, present higher runoff generation rates and coefficients than forested areas, owing to lower surface water infiltration rates (Onda et al., 2020). Additionally and in areas with cold winters, soil freeze-thaw processes increases the sediment discharge, e.g. Igarashi et al. (2021) observed on hillslopes in Fukushima Prefecture (Japan) after spring.

Soil erosion can be quantified by means of direct and indirect methods and at a wide range of spatial and temporal scales (López-Vicente and Guzmán, 2021). Plot measurements are among the most accepted methods for short-term and local assessments, mainly of sheet and rill erosion in small areas of well-known topography and geometry (Borrelli et al., 2021). USLE (Universal Soil Loss Equation) plot, which has 21 m in length and 5 m in width, has been widely used to measure net soil loss, especially in the USA (Wischmeier and Smith, 1978), but also in European (Bagarello et al., 2018), Asian (Yoshimura et al., 2015) and South American (Beniaich et al., 2022) countries, among others. However, plot measurements have the problem of the sediment delivery ratio (SDR) and plot size. Wilcox et al. (2003) observed that the specific sediment discharge decreased as the plot length increased, and Moreno-De Las Heras et al. (2010) showed that sediment discharge increased as the plot length increase on undisturbed and moderately disturbed plots, although the sediment discharge decreased as the plot length increase on disturbed plots. Parsons et al. (2006) showed that surface runoff and sediment discharge increased as plot length increase up to 4.7 m and then decreased, due to the finite travel distance and the progressive decrease in runoff coefficient. Cerdà et al. (2021) concluded that the runoff generated at the plot scale is usually disconnected from the main channel, suggesting short runoff-travel distance and duration. These results can be well described by the sediment redistribution model developed by Parsons et al. (2004), which was based on the transport distance of soil particles. To shed light on this topic, this study was focused on the processes of soil redistribution at short distances within the plot area.

Surface microtopography can play an essential role in runoff generation and soil erosion at the local scale. Small changes in soil surface structure may decrease the time to runoff initiation because the connection between small depressions cause preferential runoff (Darboux et al., 2002), although this effect is influenced by rainfall intensity, the geometry of mounds and depressions, and soil texture and bulk density (Wang et al., 2021; Liang et al., 2023). The loss of vegetation causes measurable changes in surface roughness that drastically increase particle travel distances (Roth et al., 2020). Other laboratory experiments revealed that soil surface roughness delayed the time to runoff initiation and increased the sediment concentration and clay percentage in runoff (Ding and Huang, 2017). However, Gómez and Nearing (2005) demonstrated that the effect of surface roughness on soil erosion depends on the slope gradient, with marked consequences on gentle and moderate slopes (ca. 5 %) and almost no difference on steep slopes (ca. 20 %). Microtopography can been measured with various methods like roller chain, pinboard, Terrestrial Laser Scanning (TLS), stereophoto, motion capture (Thomsen et al., 2015). TLS acquires the point clouds of soil surface structure, which has high resolution and accuracy (Barneveld et al., 2013), but it takes a lot of time on surveying microtopography on relatively large areas like hillslopes.

Quantification of microtopographic changes over time requires tracking the movement and travel distance of soil particles. Laboratory experiments have revealed that transported sediment by rain splash exponentially decrease with distances (Savat and Poesen, 1981; Torri et al., 1987). Thermal-enhanced magnetite set on the ground and tracked by measuring the topsoil magnetic susceptibility allow measuring transport distances on some lines and lattice points, but this method does not allow estimating the transport distance of individual soil particles (Armstrong et al., 2012; Parsons et al., 2010). Another methods are based on the use of high-speed cameras that are able to track the movement of sand particles one by one or clay particles with absorbed fluorescent (Furbish et al., 2007; Long et al., 2014). The use of Radio Frequency Identification (RFID) tags is an in-situ technique to measure the transport distance of individual soil particles of coarse sand size (between 2 and 5 mm of diameter). Each RFID tag can be tracked because they have a unique ID number. In the 2000s, RFID tags were used to track the movement of gravels in the river (Lamarre et al., 2005; Nichols, 2004). Recently, RFID tags were applied to soil erosion study to measure the travel distances of each particle (Parsons et al., 2014, 2018), suggesting a great potential for soil erosion survey. Coarse size soil particles are mainly transported during high intensity rainfall events (Ni et al., 2022), and thus, the accurate assessment of their travel distances will result of interest to refine the knowledge of sediment transport at the plot scale. Besides, locating RFID tags is time-consuming and a new method is needed to reduce the time to trace the RFID tags during surveys.

The recent development of Unmanned Aerial Vehicle based Structure from Motion (UAV-SfM) method has provided high-accuracy topographic data without disturbance of surface. UAV-SfM has been applied to various scales and topography such as landslide (Lucieer et al., 2014), coastal morphology (Pagán et al., 2019), and soil erosion (Kaiser et al., 2018; Stöcker et al., 2015). At the plot scale, Eltner et al. (2015) applied UAV-SfM to study soil erosion on a 5.5-degree slope and showed that the standard deviation of difference amounts (SD-diff) of height ranged between 4 and 8 mm. However, previous studies showed that the accuracy of UAV-SfM results depended on the applicability of the equipped camera to the UAV, flying height of UAV, and slope gradient (Eltner et al., 2016; Tonkin et al., 2014). The field of this study has the dimensions of a USLE plot, on a 10-degree slope, which is steeper than the conditions of the cited studies, and for this reason, our results will help to calculate the precision of this technique under medium slope conditions, complementing the existing literature about geomorphometry surveying.

Model-based approaches of structural and functional sediment connectivity are useful to map, describe and quantify the influences on the fluxes of runoff and sediment at different scales: pedon, slope, sub-catchment, watershed and basin (Parsons et al., 2015; Wainwright et al., 2011). The Index of runoff and sediment Connectivity (IC) was developed to evaluate the structural components of the landscape in the process of sediment transport, and to solve the issue of scaling in space and time (Borselli et al., 2008; Hooke and Souza, 2021). In previous studies, IC has been calculated using DEM (Digital Elevation Model) (López-Vicente et al., 2017, 2021), but the effects from high surface roughness due to vegetation need to be considered at smaller scales. In order to take them into account, it is appropriate to use DSM (Digital Surface Model) because it characterize roughness anisotropy. In the presence of an anisotropic surface texture, the resistance to flow changes according to the angle between the gradient and the direction of maximum continuity (i.e. the direction of lower roughness) (Trevisani and Cavalli, 2016). Although IC is useful for assessing sediment

dynamics at spatial scales from a qualitative perspective, quantifying these dynamics is difficult and requires specific studies at high resolution and precision (Keesstra et al., 2018, 2020).

This study aims to assess the accuracy of the UAV-SfM method to calculate soil loss and sediment transport on a plot at very fine spatial resolution by means of locating RFID tags with orthomosaic derived from the UAV-SfM method. Plot observations with a runoff collector provided data of sediment yield during different time-integrated periods, and IC was computed for each generated DEM. The use of RFID tags allowed us to track the movement of individual soil particles, which was not possible before, and to measure the sediment connectivity on hillslopes in the field using a high-resolution, high-accuracy UAV-SfM method with more detailed, low-altitude (5–10 m) images. Detailed microtopographical analysis using UAV-SfM techniques and RFID tags will clarify the connections between particle migration and sediment delivery. In addition, there is no research demonstrating the accuracy and applicability of combining the UAV-SfM method and RFID tags; and for the first time, IC and RFID are combined to improve our understanding of sediment transport at the plot scale.

2. Materials and methods

2.1. Study site

This study was conducted in a farmland hillslope located in Tsukidate, Date city, Fukushima prefecture, Japan (Fig. 1). The climate in this area is Dfa (continental with no dry season and hot summer), according to Köppen climate classification (Beck et al., 2018). According to the AMeDAS data of the Iitate station (JMA), the mean annual temperature is 10.0 °C, and the mean annual precipitation is approximately 1400 mm, with a rainy period between July and September. In September, which is the rainiest month, rainfall depth reaches ca. 200 mm, and almost half of the monthly precipitation came from typhoon events with very high rainfall erosivity (R factor). Therefore, erosive rainfall-runoff events occur during this rainy season, and cumulative R factor from July to September reaches ca. 2300 MJ mm ha^{-1} h^{-1} (Laceby et al., 2016). The highest average temperature is recorded in August ($\overline{x}$ = 22.2 °C), and the average temperature during the coldest months of winter (January and February) is below 0 °C. The selected area for this study was cultivated in the past and it has remained abandoned since the 2000s.

2.2. Hydrological observation

The experimental USLE plot of 5 m width and 22.1 m length (110.5 m^2) with 10° slope was not cultivated and kept with no vegetation by spreading weed killer. Data of rainfall, runoff, and sediment was registered every 3 weeks for a 14-week period, from 20 July to 26 October 2017. Precipitation was recorded in Tsukidate monitoring spot, which is 2 km far from Date plot. A triangular weir with a water gauge (Water Height/Temperature Datalogger, Trutrack Inc., New Zealand) was used to observe discharge at the outlet of the plot, and sediment loss was monitored with the same system as Yoshimura et al. (2015). Using a triangular weir design, two tanks (Tank-1 of 200 L; and then, Tank-2 of 200 L) were installed to trap the sediment. The deposited sediment in the triangular weir was collected with a shovel. The sediment and supernatant in Tank-1 and Tank-2 were well mixed, and the mixed water was collected to measure the suspended sediment concentration in each Tank. The sediment and hydrological data collections were conducted four times, on 2017/7/20, 2017/9/22, 2017/10/13, and 2017/10/26. Each survey corresponded to a time-integrated period. Sediment samples were dried out under 105 °C for 24 h and weighed to calculate the total sediment amount. Conversion of sediment weight (in kg) into sediment yield (in Mg/ha yr) was done considering the plot size and duration of each time-integrated period.

In order to maintain the necessary undisturbed soil conditions within the plot to perform the UAV flights, no soil samples were collected within the study area. In a previous study near Date plot, Takahara et al. (2017) collected soil samples of the upper-most layer from bare soil areas and calculated the main soil physical and chemical parameters (e.g., bulk density, particle size distribution, organic matter). Precipitation data were processed to compute the EI_{30} parameter, which represents the erosive power of rainfall and runoff of a defined period, following the approach of the USLE model to calculate the R factor (Wischmeier and Smith, 1978). Though R factor was used to assess the yearly rainfall erosivity, it can be applied to evaluate seasonally, monthly, or event erosivity, using the following equation:

$$EI_{30} = \sum_{i=1}^{n} E_i I_{30i} \tag{1}$$

where $\boldsymbol{E_i}$ (MJ ha^{-1}) is the total kinetic energy of the rainfall event $\boldsymbol{i}$, and I_{30i} (mm h^{-1}) is the maximum 30-min rainfall intensity for the event $\boldsymbol{i}$, and $\boldsymbol{n}$ is

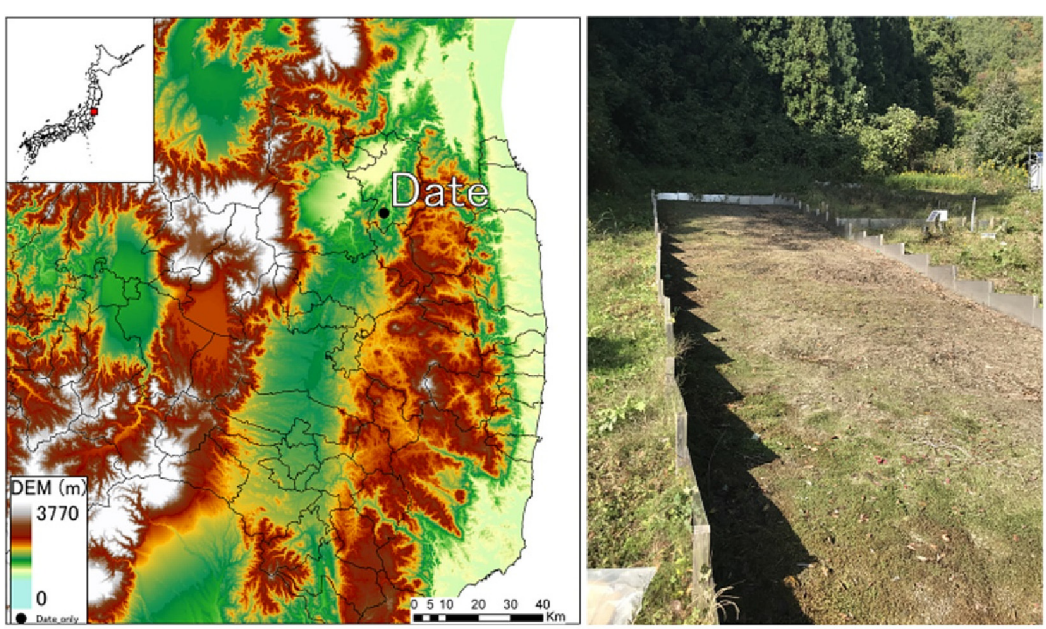

Fig. 1. Topographic map of study site and the photo of soil erosion plot.

the total number of events of the study period. When $\boldsymbol{n}$ corresponds to the total number of events in a year, then $\boldsymbol{EI_{30}}$ equals R. $\boldsymbol{E_i}$ is computed for each event as follows:

$$E_i = \sum_{r=1}^{m} e_r \, v_r \tag{2}$$

where $\boldsymbol{e_r}$ is the unit kinematic energy of rainfall (MJ m^{-2} mm^{-1}) of the shortest rainfall interval (duration of $\boldsymbol{r}$ is defined by the temporal resolution of the rain gauge), $\boldsymbol{v_r}$ is the rainfall depth of the $\boldsymbol{r}$ interval, and $\boldsymbol{m}$ is the number of intervals per rainfall event. Though some equations for the computation of $\boldsymbol{e_r}$ are provided (Renard et al., 1997), we used the one in Brown and Foster (1987):

$$e_r = 0.29[1 - 0.72\exp(-0.05\, I_r)] \tag{3}$$

where $\boldsymbol{I_r}$ is the rainfall intensity (mm h^{-1}) of the $\boldsymbol{r}$ interval; in our case $\boldsymbol{r}$ equals 10 min. Based on the time of data collection and the UAV surveys, four periods were defined: Period #0: 2017/7/20– 2017/7/27; Period #1: 2017/7/27– 2017/9/22; Period #2: 2017/9/22– 2017/10/13; and Period #3: 2017/10/13– 2017/10/26). The values of $\boldsymbol{EI_{30}}$ was calculated for each survey period.

2.3. UAV-SfM survey

Photos of the soil surface in the plot were taken by an UAV, model Phantom 4 Pro (DJI, China), which was equipped with a gimbal to stabilize the camera. The height of the flights above the ground was between 5 and 10 m, and the speed of the flight progress was kept 1–2 m s^{-1} to avoid the effect of blur. In total, 200–400 photos were taken to cover the whole plot. Each flight took 10–15 min. The four UAV-surveys were conducted on 2017/7/27, 2017/9/22, 2017/10/13 and 2017/10/26. In order to characterize the topographic map of reference, the first flight was done after removing weeds and without presence of litter (see zoomed in view in Supplementary Fig. 1).

Photos were imported to PhotoScan (Agisoft, Russia), which is a commercial SfM software, and were processed to create point cloud data. During the process, the sparse point cloud was optimised using a marker accuracy of 0.001 m and focal parameters (Fy and Fx) defined in the image headers. Camera radial and tangential distortion coefficients (K1, K2, K3, P1 and P2) were automatically estimated by PhotoScan-First –the "Align photos tool" – that detected the salient point in the photos and matched them, generating the sparse point clouds. Second, the "Build Dense cloud tool" made dense point clouds based on the sparse point clouds. Third, 15 ground control points (GCPs) were set on dense point clouds for georeferencing. These point clouds were exported to Cloud Compare (free software), and points of vegetation and biological crust were removed from them because it can affect the calculation of soil surface changes. After that, point clouds were exported as *las* format.

The obtained point clouds were used to generate the DSM of Differences (DoD) with ArcGIS Pro 2.2 (Esri, USA), using the "Las to Multipoint tool". The parameter of the average point space was set as 1 mm. Imported multipoint data were converted into Digital Surface Model (DSM) with "Point to Raster tool". We defined the cell size as 1 × 1 cm, and the z-coordinate of each cell was set as the minimum z-value of points in that cell to avoid the error caused by remained vegetation. We did not fill in the sinks of the DSM because interpolation may lead to additional errors, and thus, all depressions were considered as actual micro-topographic features. Finally, the different DSMs were used to compute DoDs with the "Minus tool".

Point cloud data of the UAV-SfM survey was assessed in comparison with 3D data derived with Terrestrial Laser Scanning (TLS). TLS used in this study was Leica Scan Station C10 (Leica Geosystems, Switzerland), which has 4 mm of accuracy of distance at 100 m away. A survey for accuracy assessment was conducted on 27th April 2017. In order to minimize missing data (e.g. a shadow of the plot walls, an area next to the device), we acquired 4 point clouds by means of locating the TLS at different places. Four data of point cloud were aligned and merged with Cyclone (Leica Geosystems, Switzerland), and the points classified as vegetation were removed manually. Noise filter and Outlier filter were applied to keep high accuracy. Point clouds derived from the UAV-SfM and TLS surveys were compared by using 'cloud to mesh tool' in Cloud Compare, which calculated the distance from the mesh data to the closest point in the point cloud. Finally, the point cloud data of the UAV-SfM was converted into mesh data to use this tool.

2.4. Calculation of the index of sediment connectivity (IC), and spatial analysis of IC

Sediment connectivity was computed in the plot by using a GIS-based index of connectivity (IC) and four DSMs that captured the surface and topographic conditions in different dates. Borselli et al. (2008) initially conceptualized the *IC* as a metric to describe the connectivity of a landscape by combining the parameters of drainage area (*A*), slope gradient (*S*), and land use and management (*C-factor*) for both the upslope (D_{up}; hillslope) and downslope (D_{dn}; drainage channel) components:

$$IC = \log_{10}\left(\frac{D_{up}}{D_{dn}}\right) \tag{4}$$

The value of *IC* ranges between $[-\infty, +\infty]$, with higher *IC* values representing greater connectivity. *IC* expresses the potential for downward routing of the sediment produced upslope and the sediment transport path length to the nearest user-defined target or sink (e.g. outlet, gully, stream system, channel, check-dam, reservoir, trail). Later, Cavalli et al. (2013) replaced the *C-factor* by the topographic roughness index (*RI*) as a proxy of the flow power in areas without vegetation cover. Lu et al. (2019) proved the usefulness of this approach in the study of time series of patterns of rill channel confluences and depressions (structural disconnectivity). The upslope component D_{up}, denoting the routing of sediment from contributing upland, is defined as:

$$D_{up} = \overline{W}\,\overline{S}\,\sqrt{A} \tag{5}$$

where $\overline{W}$ is the average weighting factor, $\overline{S}$ is the average slope, and *A* is the size of the upslope drainage area. The downslope component D_{dn}, denoting the path of the sediment from any cell to the computational target –the outlet in this study–, is defined as:

$$D_{dn} = \Sigma_i \frac{d_i}{W_i\, S_i} \tag{6}$$

where d_i is the flow path for the ith cell in the steepest direction downslope (m), W_i is the weighting factor, and S_i is the slope gradient of the ith cell. S and $\overline{S}$ were set to a minimum value of 0.005 and a maximum value of 1.000 m/m to avoid computational errors (when *S* equals zero) and the overestimation of the effect of very steep areas. Following the approach of Cavalli et al. (2013), we used a local measure of the topographic surface roughness, the so-called roughness index (*RI*), to calculate the weighting factor *W*. This approach is suitable for calculating the anisotropic roughness of the surface features, i.e. the flow directional impedance. *RI* is defined as:

$$RI = \sqrt{\frac{\Sigma_{i=1}^{25}(x_i - x_m)}{5 \times 5}} \tag{7}$$

where 25 is the number of the processing cells within the 5 × 5 cells moving window, x_i is the value of one specific cell of the residual topography within the moving window, and x_m is the mean value of the residual topography of the 25 cells values. The weighting factor *W* is calculated as:

$$W = 1 - \left(\frac{RI}{RI_{max}}\right) \tag{8}$$

where RI_{max} is the maximum value of RI within the study area. A lower limit of 0.001 was set to avoid $W_i = 0$ in the computation of D_{dn}. In this study, index setup and calculations were done using ArcGIS Pro 2.5 (Esri, USA).

To refine the results analysis, a geostatistical analysis was conducted to assess the differences in connectivity patterns between the inter-rills, rills and depositional-prone areas. At first, a point-type shapefile with 200 random points were created using ArcGIS Pro. Then, the values of IC for each temporal scenario using the 200 random points were extracted (800 points data in total), and used to calculate the relative difference (δ_{it}) between IC at each random point 'i' (IC_{it}) and the average value ($\overline{IC_t}$) at each temporal scenario 't':

$$\delta_{it} = \frac{IC_{it} - \overline{IC_t}}{\overline{IC_t}} \tag{9}$$

The analysis of the temporal series included the calculation of the mean relative difference (*MRD*), standard deviation of relative difference (*SDRD*), and coefficient of variation of the relative differences (*CVRD*):

$$MRD_{iT} = \frac{1}{N_T} \sum_{t=1}^{t=N_T} \delta_{it} \tag{10}$$

$$SDRD_{iT} = \sqrt{\frac{1}{N_T - 1} \sum_{t=1}^{t=N_T} (\delta_{it} - MRD_{iT})^2} \tag{11}$$

$$CVRD_{iT} = \frac{SDRD_{iT}}{|MRD_{iT}|} \tag{12}$$

where N_T is the number of observation times (4 times). The orthomosaic, which is a photogrammetrically orthorectified image product mosaicked from the UAV-SfM image collection, were generated at 1 × 1 mm of cell size and used to classify the areas between the inter-rills, rills and the depositional-prone areas.

2.5. Sediment tracing with RFID tags

Radio frequency identification (RFID) tag is an indirect method to calculate sediment connectivity. In this study, we used a RFID tag made by Hitachi Chemical (IM5-PK2525, Japan) (Fig. 2a). Each tag has a size of 2.5 × 2.5 × 0.375 mm, which is comparable to the size of the quartz grains that is 3–5 mm. To make the detection length of RFID tags longer, we attached the coil to the RFID tag (Parsons et al., 2018). As the RFID tag is different from soil particles in shape and density, we coated RFID tag with cement and bronze powder (Fig. 2b). The density of this coated RFID tag was 2.0–3.0 g cm^{-3}, which is similar to the density of the soil coarse fragments. Additionally, we painted these tags with fluorescent, in order to facilitate the tracing of the tags, and coated with glue to make tags stronger.

We set 100 RFID tags on the plot on 27 July 2017 on nine cross-sections located 1, 3, 5, 7, 9, 11, 13, 15 and 17 m from the boundary of the plot, and along one rill. The location of the RFID tags was identified with an orthomosaic derived from the UAV-SfM survey. As RFID tags were sometimes challenging to find in the orthomosaic, we used the self-made targets (Fig. 2c). This target is made of a bamboo skewer and about 2 cm-ball of Styrofoam and is about 18 cm in length. We set targets close to the RFID tags before taking photos with UAV (Fig. 2d). Though the number was written on the ball of the target, we roughly recorded the location of the RFID tags in case of missing numbers in the orthomosaic. Photos of the targets and RFID tags were taken after setting the targets and used to create the point clouds with the same method as topographic measurement. After point cloud was georeferenced with some GCPs, the different orthomosaics were created with PhotoScan and were imported with ArcGIS. We looked for the targets or RFID tags in the orthomosaic and get the XY-coordinates of all RFID tags. The *Z*-coordinate of the RFID tags were added by extracting the value of the DSM at the location of each RFID tag.

After locating the RFID tags, they were classified into two groups, those located in the interrill areas and those in the rills. The rill area was defined as the range of 10 cm from the overland flow network, which was obtained with the DSM and ArcGIS Pro tools. First, interpolated DSMs were generated by processing point clouds using the Natural Neighbour method of interpolation. These interpolated DSMs were smoothed with "fill tool". Then, the flow direction and flow accumulation raster maps were generated. Finally, we extracted the cells from the flow accumulation raster whose value extended 40,000 cells and converted them into the stream network. The accuracy of this method to locate the RFID tags was assessed in comparison with the XY-coordinates derived with the total station (TS) on 27th April 2017. We did not consider the accuracy of the Z-coordinate because it depended on the accuracy of the DSM. TS used in this study was Tajima laser total station (TT-2017, Tajima Corporation, Japan) with an accuracy of distance of 1.5 mm. Twenty-seven targets were set on the plot. One target was excluded because we failed to locate it with TS. Therefore, 26 points were assessed.

3. Results and discussion

3.1. Accuracy of the 3D data

The accuracy of the point cloud derived with the UAV-SfM method was analysed in two points. Errors on GCP were summarized in Table 1. The root-mean-square errors (RMSEs) at the GCPs in the x-axis (slope crossing direction), in the y-axis (slope direction) and z-axis (vertical direction) were calculated, and the accuracy was very constant over time. The ranges of the errors of the x-, y-, and z-axis varied between 3.1 and 4.4 mm, 4.1–4.8 mm, and 1.5–2.7 mm, respectively.

Fig. 3a shows a comparison of 3D data between the UAV-SfM (10 × 10 mm of pixel size) and TLS surveys (4 mm of accuracy). Both methods are based on different techniques of ground characterization and image analysis, but they are all affected by the local changes of soil bulk density; therefore, the comparison of the outputs of the two can be considered as a correct procedure. In this study, the TLS survey was taken as the true value and the error of the UAV-SfM DSM was calculated. The average and the standard deviation of all investigation intervals was calculated. In Fig. 3, the light green region represents the small differences, and the red or blue areas represent the significant differences. When the camera pre-calibration was not performed in the PhotoScan settings, the difference amounts around the centre were large when importing the photos from the Phantom 4 Pro at first, because the error caused by the lens was propagating and reflections occurred. Later, the dishing phenomenon was no longer observed when the camera was pre-calibrated. Almost all areas showed minor differences in the plot. Points in the upslope area and near the plot wall were sparser (2.5 points cm^{-2}) than another area (20 points cm^{-2}) on the TLS survey because of the shadowing effect produced by the small ridges or the plot wall, and the unfavourable low viewing angle onto the plot.

The histogram of these errors, defined as the distance –deviation– between the point cloud derived with the TLS survey and the mesh converted from the point cloud derived with the UAV-SfM survey, is shown in Fig. 3b. The gray line shows the Gaussian distribution calculated from the mean and standard deviation. This graph exhibits a normal distribution, and the average of the difference is 0.1 mm, and the standard deviation of difference amounts (SD-diff) is 3.3 mm. This value coincides with that of the 3D data derived from the UAV-SfM survey done at a similar height (8–11 m) (Eltner et al., 2015). These authors compared the TLS and UAV-SfM surveys with the open-source solution CloudCompare –the same method used in this study– and judged that all 3D data obtained in their study was satisfactory in terms of accuracy.

An additional analysis of the products generated in this study included the comparison of the hillshade images (1 mm cell size) with the longitudinal profile extractions of the TLS and UAV-SfM surveys-derived DSMs (Fig. 4). In both surveys, we compared hillshade images and longitudinal profile extractions of the surface structures at 5, 10 and 15 m from the

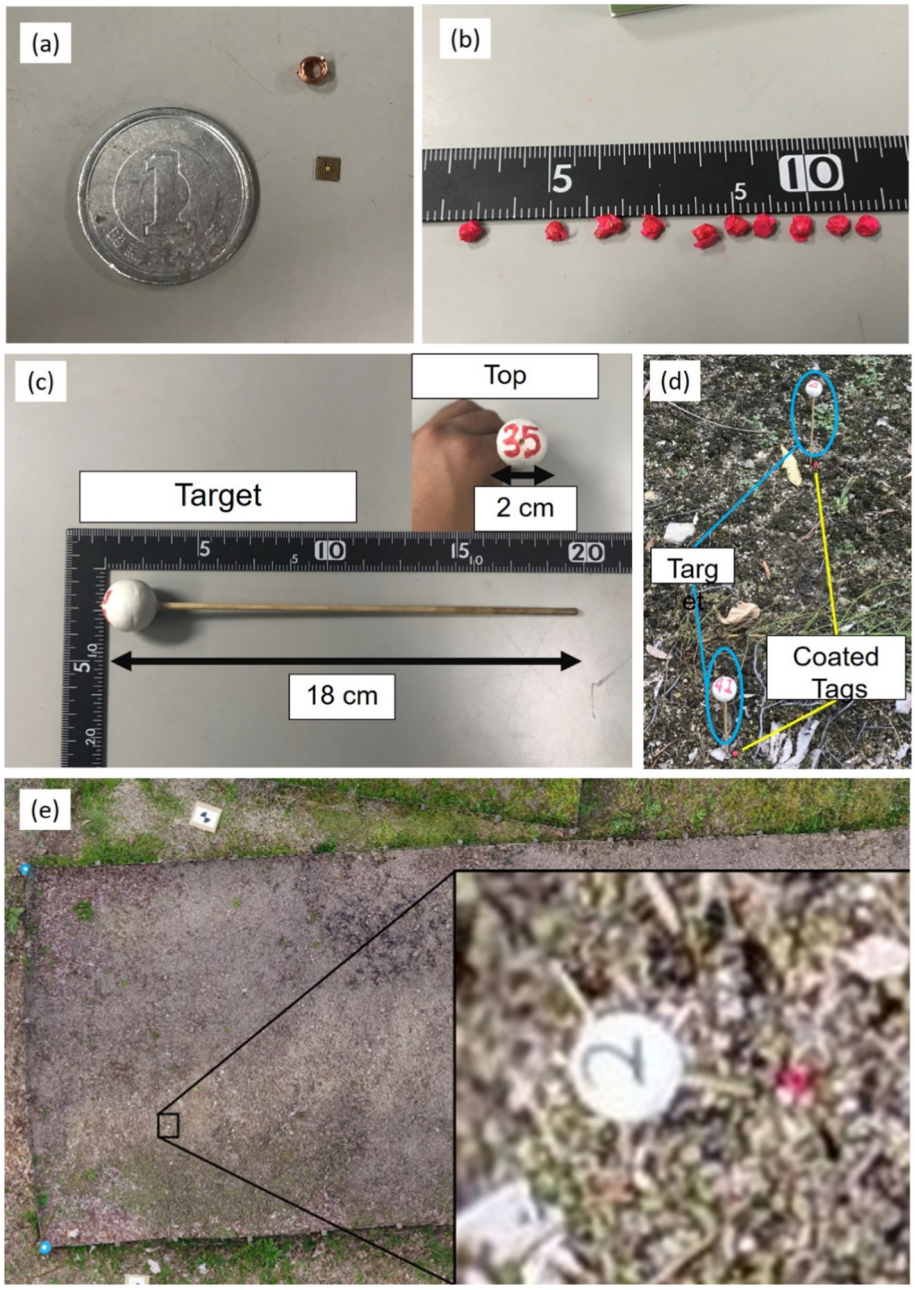

Fig. 2. The use of RFID tag in the field. (a) RFID tag used in this study and the anntenna attached to tag. (b) RFID tags coated with cement, bronze powder, fluorecent, and topcoat. (c) Targets for locating RFID tags with orthomosaic. (d) Targets set on the field plot. (e) Orthomosaic and expanded image of the target and RFID tag.

bottom of the plot. This comparison showed that the TLS survey method was better at representing the microtopography. However, the comparison of the longitudinal profile extractions of the surface structures showed that the maximum error was 2.0 cm and the average error was 0.1 mm. Therefore, the UAV-SfM profiles did not show a great difference on profile extractions, which supported the accuracy of the UAV-SfM survey. Glendell et al. (2017) estimated soil loss –in 10 sites with different land uses and soil types, with special interest in gullies– from UAV-SfM and TLS reconstructions, finding comparable rates. Cucchiaro et al. (2020) produced very high-resolution digital terrain models (DTMs) of two agricultural terrace areas by means of using SfM–TLS data fusion methodology, and proved that data fusion was required to obtain accurate DTMs that reflected the real surface roughness without gaps.

Table 1
Root-mean-square errors (RMSEs) of the SfM point cloud data (xyz coordinates) calculated at the 15 ground control points (GCPs) with the TLS.

Date of the orthomosaic	Jul. 27, 2017	Sep. 22, 2017	Oct. 13, 2017	Oct. 26, 2017
End of the Period	0	1	2	3
X (mm)	3.9	4.4	3.1	3.7
Y (mm)	4.1	4.6	4.8	4.7
Z (mm)	1.5	2.2	2.7	2.5

3.2. Locating the RFID tags with the orthomosaics

Fig. 5 shows the histogram of the errors of the method to locate the RFID tags using an orthomosaic, comparing with the laser total stations (TS). Histograms of errors were created in (a) slope crossing direction, (b) downslope direction, and (c) linear distance. The linear distances between the coordinates of the different RFID tags were derived with the orthomosaics and with the total station. The RMSE for the slope crossing

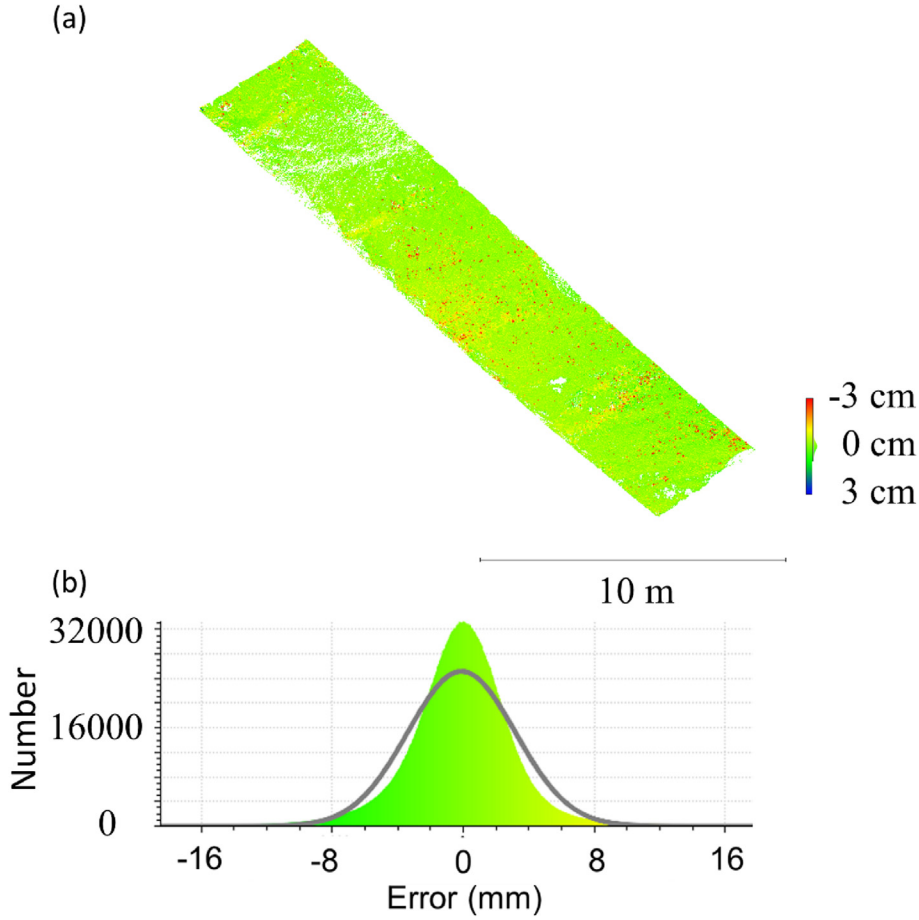

Fig. 3. Standard deviation of the difference amounts (SD-diff) of UAV-SfM survey from 5 to 10 m height, compared by TLS survey. (a) 3D map of calculated error, left-bottom side shows downslope. (b) The histogram of calculated error. Gray line is fitted curve with normal distribution.

direction was lower ($\overline{x} = -0.012$ m, RMSE = 0.017 m, $n = 25$) than the RMSE for the slope direction ($\overline{x} = 0.017$ m, RMSE = 0.026 m, $n = 25$). The RMSE of the linear distance was 0.031 m (Fig. 4). The RMSE value at target for locating the RFID tags (= 0.011 m, evaluated with TS data) was more significant than that at the GCPs (= 0.031 m, evaluated with TLS).

This results may be due to several reasons. Firstly, the effect of the tilting of the target for the RFID tags could increase the RMSE values. No specialized tools were used to check whether the target was inserted perpendicular to the soil surface by hand. That's why the direction of the embedded targets may be shifted and increased the error to locate the RFID tags. Second, the inserted direction of targets for the RFID tags could also cause errors. The targets were set perpendicular to the soil surface, and the orthomosaic was created perpendicular to the xy–plane, which was defined with the GCPs. This procedure may cause an error in the direction of the slope. In fact, the RMSE value in the slope direction was higher (0.026 m) than that in the slope crossing direction (0.017 m) (Fig. 5), which indicate the effect of the slope on the accuracy of the target measurement. Third, the error at merging the orthoimages into the orthomosaic. In order to build the orthomosaic in PhotoScan, the *Mosaic* option was selected as blending mode. *Mosaic* option combines the values of pixels on the same line (Agisoft, 2017), and this procedure may make it hard to find the centre position of the targets. The final possibility is the effect of the wind-driven by the UAV. Because the UAV was controlled by hand in this study, flying height above the ground sometimes became below 3 m. Flying at low height may cause wind gusts downward, and the targets for locating the RFID tags could be moved or shaken. Therefore, the wind may alter the position in the aerial photos and contribute to increasing the RMSE value for determining the RFID tags using the orthomosaics.

3.3. Sediment transport processes

3.3.1. Runoff yield

Fig. 6 shows the recorded values of precipitation and runoff yield during the study period. The hydro-hyetograph showed two main discharge events. During Period 1, nine rainfall events with high rainfall intensity happened and caused the flush at the plot at the end of July. During Period 3, Typhoon Lan came to Fukushima prefecture, and it rained continuously for 4 days. At the end of this event, runoff from the plot was observed. Parameters of rainfall, runoff and sediment are presented in Table 2. EI_{30} and total precipitation showed similar values in Period 1 and 3. However, I_{30max} was higher in Period 1 than Period 3, and the peak runoff was higher in Period 3 than Period 1. We focused on this difference in the rainfall pattern below.

Surface changes for periods 1, 2 and 3 were shown in Fig. 7. The top side of the graph was the upper slope in the field. The red area showed the surface rising, which means sedimentation, vegetation growth, or animal activity like moles. The blue area showed the surface lowering, which means net soil loss, vegetation withering, or animal activity. Assuming that the soil density in the plot was 1.6 g/cm^3 (data source: Takahara et al., 2017) and using the maps of surface changes, the estimated weight of soil lost was of 0.298, 0.013 and 0.708 Mg at the end of the Period 1, 2 and 3, respectively. These rates were very high (37.3, 1.6 and 88.5 Mg/ha for Period 1, 2 and 3) and lower density values (< 1 g/cm^3), associated with the increase in plant remains in the successive periods and, above all, with the presence of disaggregated soil, would give rise to lower rates of net loss (22.1, 0.9 and 52.5 Mg/ha for Period 1, 2 and 3). This aspect requires further research activities. Minor changes were detected in Period 2 and this fact could be explained by the low rainfall depth observed in this period (Table 3). On the other hand, soil surface changed in a different way in Period 1 and 3. The surface change in Period

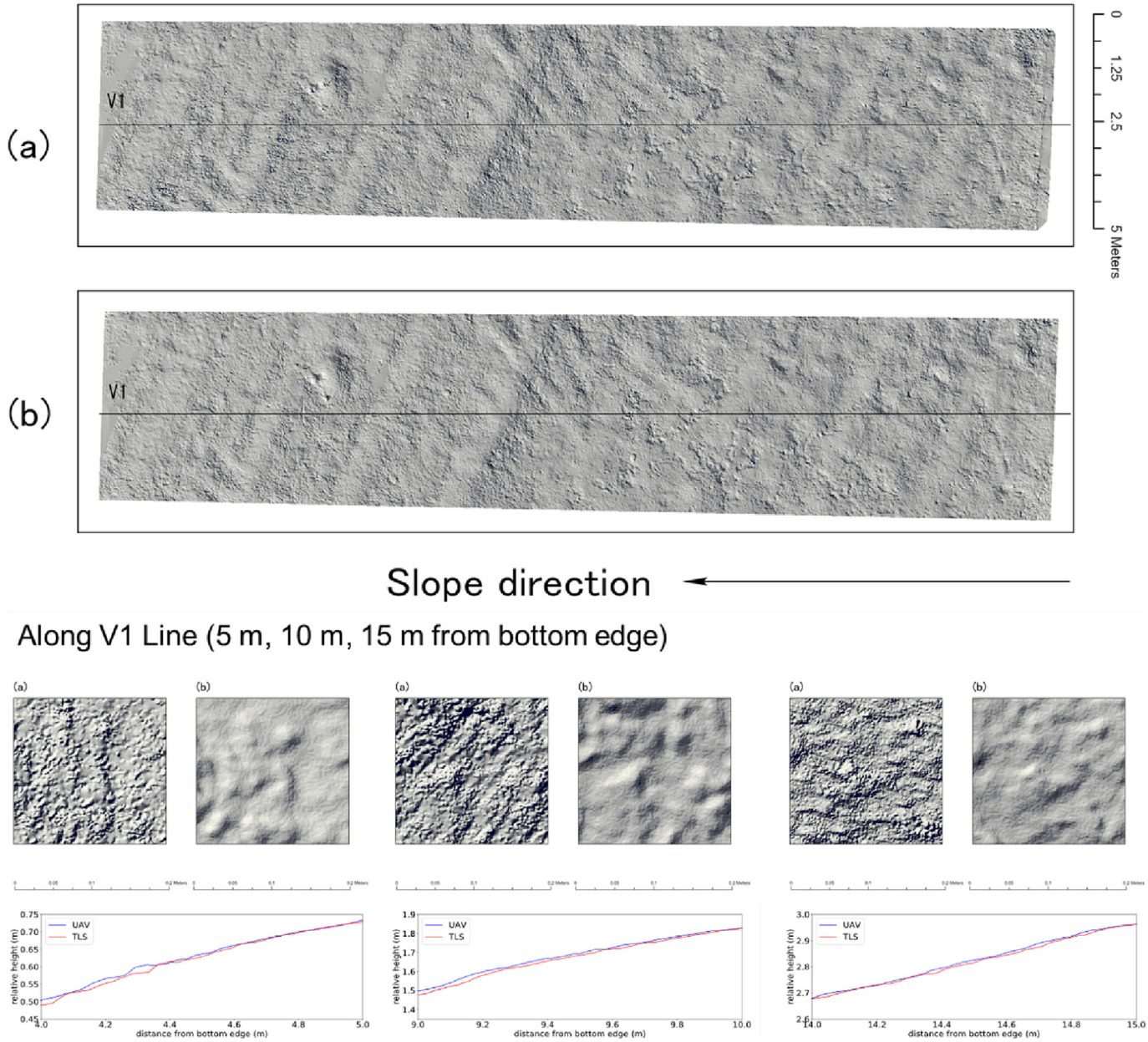

Fig. 4. Comparison of hillshade images (1 mm cell) with longitudinal profile extractions of TLS and UAV-SfM surveys from DSM. (a) shows TLS survey. (b) shows UAV-SfM survey.

1 showed both lowering and rising, and that in Period 3 showed decreasing and less rising. The figure of soil surface changes at the middle slope was expanded to show the detailed distribution of changes in Period 1 and Period 3 (Fig. 8). In Period 1, surface lowering caused by rill erosion was detected, and just below that, surface rising by sedimentation seemed to exist. On the other hand, in Period 3, the surface rising of deposition below the surface lowering was not detected, and thus, a net soil loss and sediment delivery outside the plot was inferred. The aerial photos of the expanded area are showed in Fig. 8. These images showed that in the periods #1 and #3, the rill topography was observed, but the depositional structure below the slope of the rill was only observed in Period 1, and in Period 3, the lateral flow was observed (Fig. 8c,d).

3.3.2. Sediment connectivity

Regarding sediment connectivity, the maps of IC were analysed taking into account two aspects: I) the evolution of the mean ($\bar{x}$), median ($\tilde{x}$), minimum and maximum values; and II) the spatial pattern of the areas with high and low connectivity. The mean and median values did not show a clear trend, and comparable values were found among periods: Period 0 ($\bar{x} = -4.274$, $\tilde{x} = -4.337$), Period 1 ($\bar{x} = -4.057$, $\tilde{x} = -4.121$), Period 2 ($\bar{x} = -4.099$, $\tilde{x} = -4.160$), and Period 3 ($\bar{x} = -4.112$, $\tilde{x} = -4.188$). The maximum values varied slightly between -0.92 and 0, but the minimum values clearly increased from Period 1 (-9.250) to Periods 2 (-8.440) and 3 (-7.545), indicating a reduction of the areas with low values of connectivity. These results suggested that the different rainfall events registered over the study period did not alter significantly the conditions of surface microtopography in terms of surface roughness, and thus, the values of the roughness index –*RI* in Eq. (7)– were not much affected.

However, clear changes appeared in the spatial pattern of IC between the four maps, with respect to the location, extension and number of areas with high/ low connectivity (Supplementary Fig. 2). Based the spatial analysis on the map of IC for the Period 0, the number and extension of areas with high connectivity increased near the outlet, whereas little changes appeared near the top positions of the plot. Between Period 2

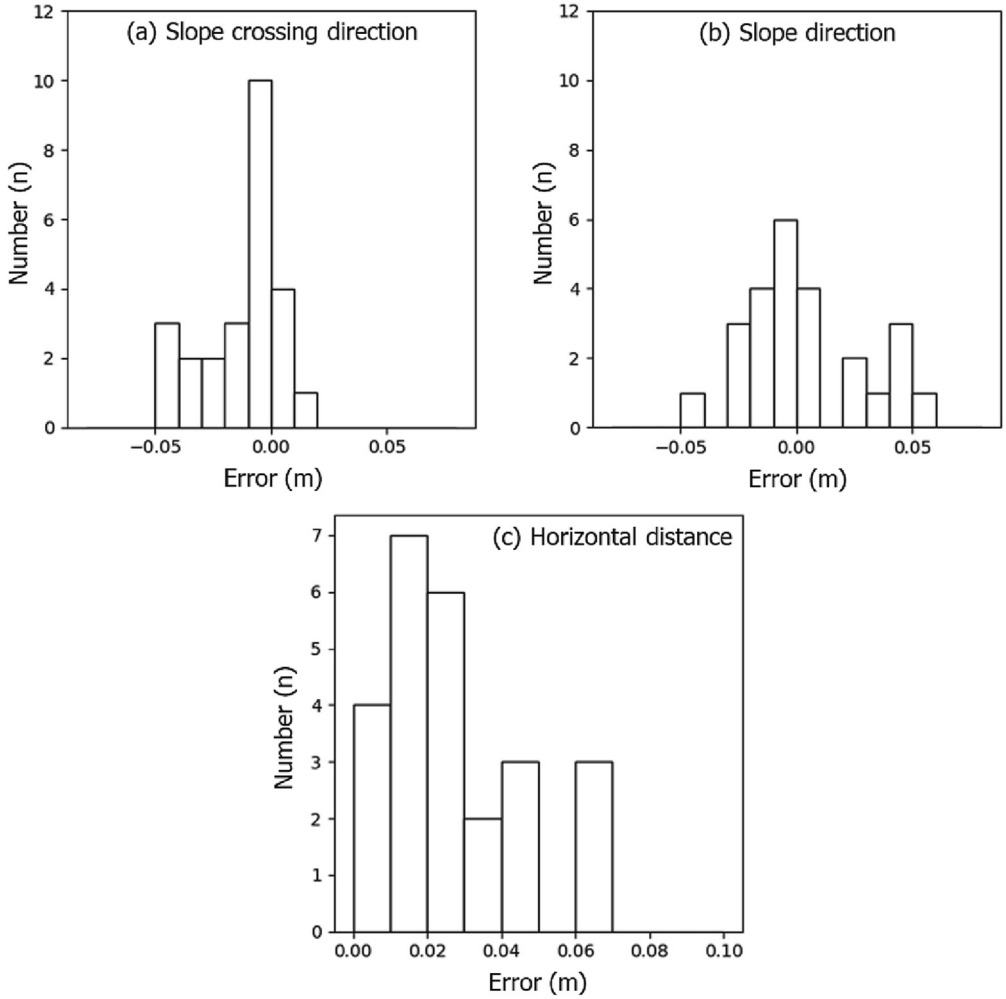

Fig. 5. Histogram of errors of locating RFID tags with orthomosaic derived with UAV-SfM survey. Coordinate data derived with TS were used as reference data.

and Period 1, minor changes were observed and quite similar patterns appeared in the connected and disconnected areas. However, the IC map of Period 3 showed new connections between the rills formed by the surface flow from the top and lateral surface flow, describing a pattern of longer rills, compared with the rills identified in the periods 0, 1 and 2. In Period 3, the length of the overland flow network with high connectivity reached the maximum values, especially in the rills located in the middle part of the plot (Fig. 8e,f). The maps of the periods 0, 1 and 2 showed areas with low connectivity or disconnected areas, that appeared distributed throughout the plot. These depositional areas showed high connectivity upwards and low connectivity at the local scale, due to the presence of weeds with the expected effect of high surface roughness. Those areas that acted as disconnected areas in the previous periods that appeared as connected areas in Period 3 can be considered as functionally connected areas following the approach of (Martini et al., 2022). These authors considered these areas as connected with the main stream system, but specifically referring to an event-based type of linkage. Therefore, the functionally connected areas identified in Period 3 showed field evidence of sediment transfer associated with the Typhoon Lan, rather than a permanent interface. These sources of sediment will probably stabilize in the near future.

The geostatistical analysis of the IC maps (see Eqs. (9)–(12)) showed the clear variation over the whole study period in the three geomorphological features: Rills, inter-rills and depositional areas (Table 3). Rills had the highest values of sediment connectivity, with moderate spatial homogeneity and low temporal stability. In the inter-rill areas, which is the other soil erosion-prone feature, sediment connectivity was characterised by the lowest values, because of the highest spatial heterogeneity and low temporal stability. Showing an opposite pattern, the depositional-prone areas presented low values of sediment connectivity, and these values were homogeneous across space and stable over time.

3.3.3. Travel distance with the RFID tags

During the four surveys to measure the transport distance of the RFID tags, a decrease was observed in the number of tags: The recovery rates were 66 %, 62 % and 49 % at the end of the periods 1, 2 and 3, respectively. The missing particles may be washed away and most likely buried below the soil. The last hypothesis was demonstrated by Kayad et al. (2019) in arable land, where they found high chance of RFID tag burial when soil was removed. Our recovery ratios were similar to those obtained in past studies; e.g. Parsons et al. (2014) measured transport distance of RFID tags between 20th July and 31st October 2012, almost the same period as this study, and the recovery rate was 44 % at the end of their study.

Transport distances (TD) of the RFID tags were calculated for each period. Fig. 9 shows the histograms of TD for all particles, and the particles located in the interrill areas and rills, including the max, mean and median TD. Period 1 showed more extended TD in both the interrill and rill areas than Period 2 and 3, and the shapes of the histograms of interrill and rill were different. The histogram of Period 2 showed that TD of almost all particles were <0.1 m (95 %), and there was no significant difference in histograms of the interrill areas and rills. As expected, Period 3 showed more extended TD than Period 2, but a significant difference was not found in the histogram of the rill and interrill area, maybe due to the small size of the plot.

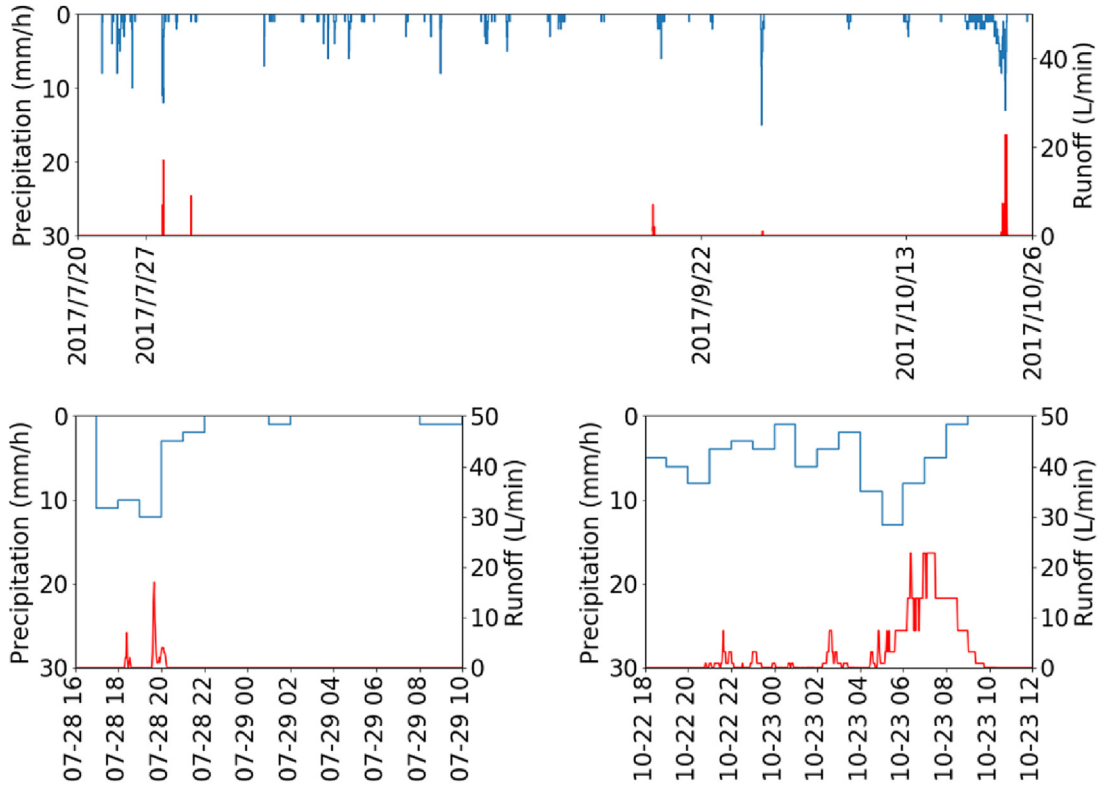

Fig. 6. Time series of rainfall (blue lines) and surface runoff (red lines). (a) data for whole study periods. (b) data for 2017/7/28–7/29, which has high rainfall intensity (max 8 mm in 10 min) and runoff. (c) data for 2017/10/19–10/23, when Typhoon Lan struck Japan during this period.

To refine the results analysis, the splash transport model was applied to the histogram of TD of the RFID tags. Past studies tested how far the soil particles were transported by raindrop splash in the laboratory and they suggested that the splash transport model can be explained by the mean TD (Furbish et al., 2007; Long et al., 2014; Savat and Poesen, 1981; Torri et al., 1987):

$$\frac{M(r)}{\mu} = \frac{1}{\bar{r}} exp\left(- \frac{r}{\bar{r}}\right) \tag{13}$$

where $M(r)$ is the transported sediment to the point, μ is the amount of detachment, r is the transport distance, and $\bar{r}$ is the mean transport distance.

We assumed that the probability of TD is the same as $M(r)$ divided by μ, and splash transport model was fitted with the mean TD to the histogram of TD. The fitted models were shown as a solid line in the histograms (Fig. 9). For the histograms of the interrill areas, the splash transport model was well fitted. However, for the histograms of the rills, the splash transport model was well fitted in Period 2 and 3, but not showing a similar tendency in Period 1, which suggested a difference magnitude in the sediment transport process. In the interill areas, splash transport can dominate because the histogram of TD was well fitted with a splash transport model. On the other hand, the histogram of TD of the rills in Period 1 showed a long-tailed form and did not fit with the splash transport model, which can result from flow transport.

3.3.4. Sediment dynamic over the distinct periods

Sediment transport systems were compared between Period 1 and Period 3. Period 2 was excluded because minimal sediment discharge (0.6 Mg/ha yr) and soil surface changes were observed (Fig. 7, Table 2). When the sediment transport process in the interrill area was focused on, that in Period 1 should be explained by higher activity of sediment detachment and transport (2.3 Mg/ha yr). Gabet and Dunne (2003) showed the positive relationship between rain power and sediment detachment rate divided by the parameter of flow depth. Some physical models also included the negative effect of flow depth on the detachment rate (Hairsine and Rose, 1991; Parsons et al., 2004; Wainwright et al., 2008). In period 1, higher rain power and less flow depth was inferred because higher rainfall intensity and less total and peak runoff were observed (Table 2). Accordingly, sediment detachment in the interrill area in Period 1 was higher than that in Period 3. The transport of the RFID tags in the interrill area and splash transport model showed the more extended sediment transport in the interrill area. We considered that the flow depth also explained these results because Ghahramani et al. (2012) showed that maximum transport distance was related to the total precipitation, and Torri et al. (1987) showed that higher flow depths decreased the rates of soil detachment and transport by splash.

The differences in sediment discharge among periods were explained by the combination of soil detachment and transport, and sediment connectivity. Period 1 showed less sediment discharge (2.3 Mg/ha yr) than that in

Table 2
Results of hydrological observation.

Period	Precipitation	I30 max	Number of Events	Total Event Duration	EI30	Total runoff	Peak runoff	Sediment weight	Sediment yield
	mm	mm h^{-1}	n	min	MJ mm/ha h period	L	L/min	Kg	Mg/ha yr
0	71	18	3	2640	159.5	0	0	4.52	2.3
1	218	22	6	5010	354.3	290	17		
2	64	16	1	790	115.7	114	1	0.39	0.6
3	197	14	1	6410	398.9	3287	23	18.72	47.6

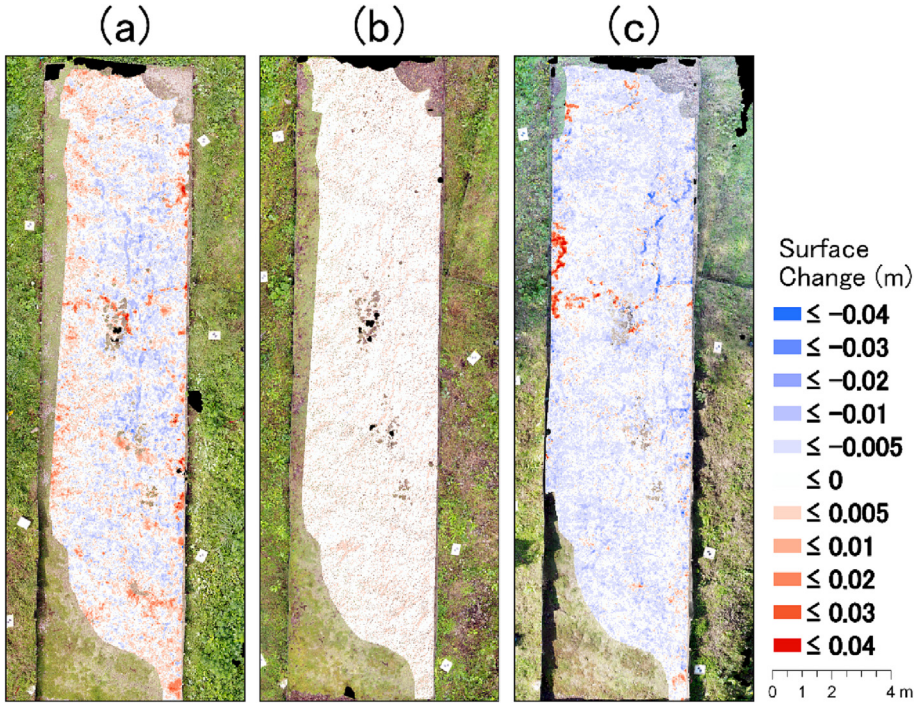

Fig. 7. Surface changes for (a) period 1, (b) period 2 and (c) period 3.

Period 3 (47.6 Mg/ha yr), even though rill incision occurred and the intense process of sediment detachment and transport in the interrill areas (Figs. 7-9, Table 2). The differences in sediment connectivity resulted in lower sediment discharge rates in Period 1 than in Period 3. The sediment transport in the rill area was longer in Period 1 than in Period 3 (Fig. 9), suggesting that more transport of sediment occurred via rills. However, the maximum transport distance in Period 1 was below 2 m (= 1.94 m). Besides and in the rill area, we found only 5 particles in Period 3, which was a much lower number than the 15 particles found in Period 1 (Fig. 9), stressing that sediment transport and flowing out of the plot was more intense in Period 3. Comparison of surface changes and aerial photos between Period 1 and 3 showed the occurrence of sediment deposition in Period 1 downslope of the rill incision (Fig. 8). Higher sediment detachment and transport in the interrill areas and rill incision could produce more sediment load, but the depositional area can stop the sediment and lead to less sediment discharge, suggesting a predominance of short distances in the transport of eroded soil particles.

The RFID tracing data (focussed on coarse soil particles) showed a short transport distance associated with rill erosion, but the results of UAV-SfM surveys, which reflects the result of different combined processes, but does not quantify the role of each process separately, showed higher connectivity that contributes to large sediment discharge from the plot. Therefore, our results highlighted the relevance of combining the RFID tags and UAV-SfM methods together with the IC to improve our understanding of the different processes acting in soil erosion over the course of different rainfall-runoff events. As a result of this combination, the movement of individual soil particles was able to be tracked, revealing the connectivity between soil particles movements and deposition.

Table 3
Geostatistical analysis of the relative differences of IC in the rills, inter-rills and depositional-prone areas.

Feature	*n*	MRD	SDRD	CVRD
Rills	67	0.0234	0.1308	343 %
Inter-rills	108	−0.0141	0.1478	341 %
Depositional-prone areas	25	−0.0018	0.1172	158 %

This study demonstrated the accuracy (Acc.) and applicability of the combined use of the UAV-SfM (Acc. = 3.3 mm) and RFID tags (Acc. = 3.1 cm) methods, together with the IC (microtopography approach) to study the complexity of soil erosion processes at the plot scale. In particular, the role played by the surface roughness on rill and interrill soil loss, sediment delivery and yield, and the occurrence of depositional (disconnected) areas. In addition, survey time for determining 100 RFID tags decreased by about 80 % compared with previous studies (Total station: 100 min, UAV-SfM: 20 min). Further studies will look into the analysis of transport of the RFID tags and the study of sediment connectivity at very high resolution (1 cm or less) by using accurate DSMs that capture all features lying on the ground, including the height and volume of weeds and litter. The presence of small disconnected areas, induced by natural or man-made elements, plays an important role in the processes of temporal storage of sediment and sediment transport at short distances (López-Vicente et al., 2021). Therefore, the generation of accurate DSMs appears as a relevant task in the study of soil redistribution in both cultivated and non-arable lands.

4. Conclusions

This study has proven the high accuracy of the UAV-SfM method (flight altitude from 5 to 10 m) to study soil erosion and transport in a 10-degree slope USLE plot (5 m width × 22.1 m length) and that of locating RFID tags with orthomosaics derived from the UAV-SfM method. First, the accuracy of the UAV-SfM survey was assessed by comparing it with the TLS survey, and the standard deviation of difference amount (SD-diff) was 3.3 mm. Second, RFID tags were located with the orthomosaic, and the accuracy of this method was assessed by comparing it with the TLS survey, which resulted in the error of 3.1 cm (horizontal RMSE value). By means of using UAV-SfM images to assess sediment tracing with the RFID tags, the method reduced the time from a few hours to 20 min to trace the RFID tags during the field experiment.

The combined use of the UAV-SfM method, tracing the RFID tags and the maps of sediment connectivity (generated with the roughness index IC approach) allowed evaluating the distinct sediment dynamic observed in the different rainfall-runoff events. Over the four periods of this study, the differences in the magnitude and role played by the processes that

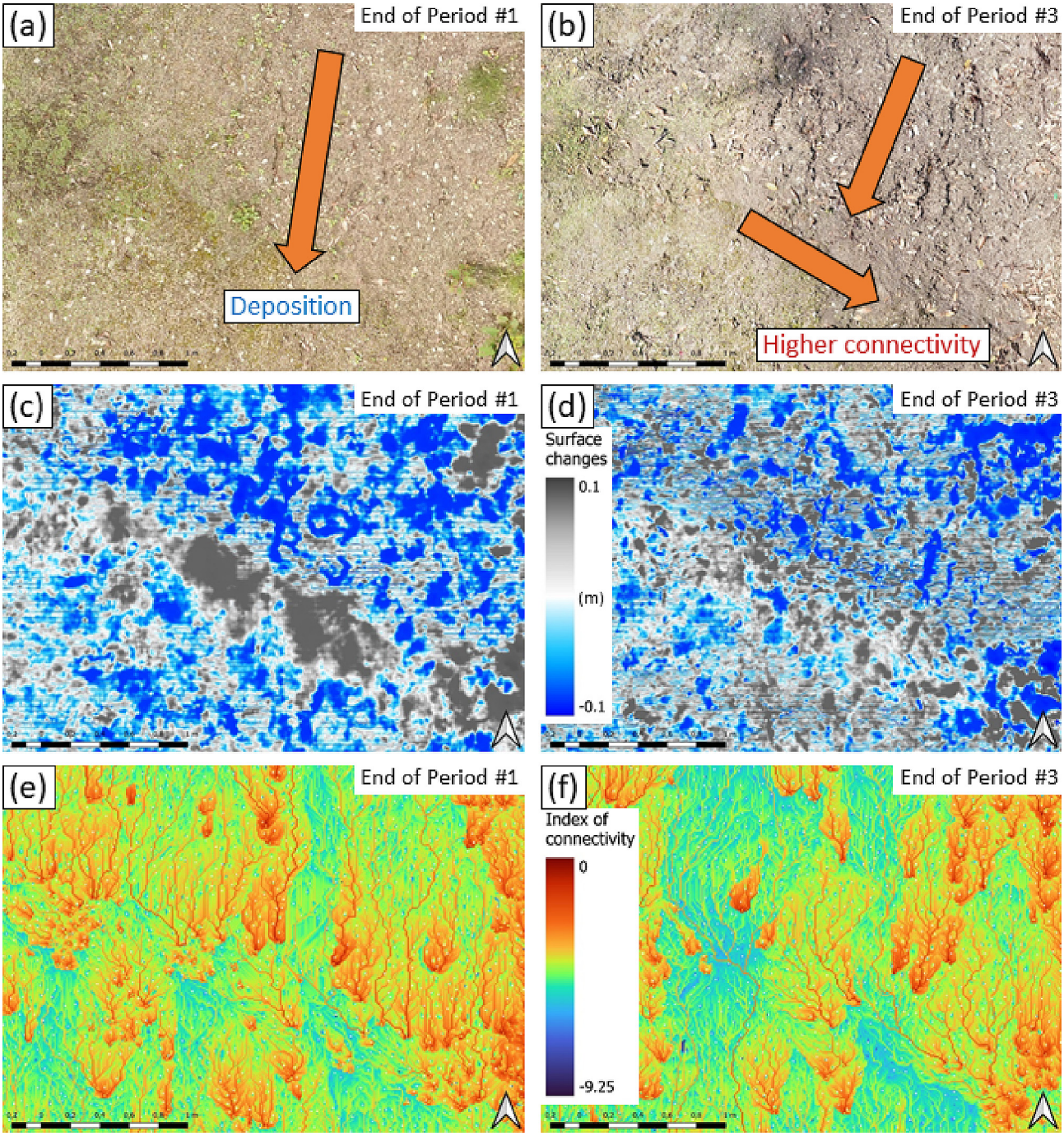

Fig. 8. Zoom-in view of an area, showing the mosaics (a, b), surface changes (c, d) and maps of sediment connectivity (e, f) at the end of the periods 1 (a, c, e) and 3 (b, d, f).

took place in the rills, interrill areas, and depositional zones were characterised and evaluated. Our findings proved that distance of travel appeared as a relevant component of the soil erosion process that explained the observed sediment yield over the study period, regardless the magnitude of soil erosion observed in the interrill areas and rills. Therefore, the combination of distinct techniques gave us an indication of the difference in the sediment transport process between different erosion processes.

Supplementary data to this article can be found online at https://doi.org/10.1016/j.scitotenv.2023.164545.

CRediT authorship contribution statement

Investigation, Formal analysis, Methodology, Software, Interpretation of data, and Writing and original draft: Manuel López-Vicente, Seigo Fujiwara, Yuichi Onda, Shohei Kozuka, Yoshifumi Wakiyama, and Hiroaki Kato. Conceptualization, Funding acquisition, Supervision, Project administration and Data curation: Yuichi Onda.

Data availability

Data will be made available on request.

Declaration of competing interest

The authors declare that they have no known competing financial interests or personal relationships that could have appeared to influence the work reported in this paper.

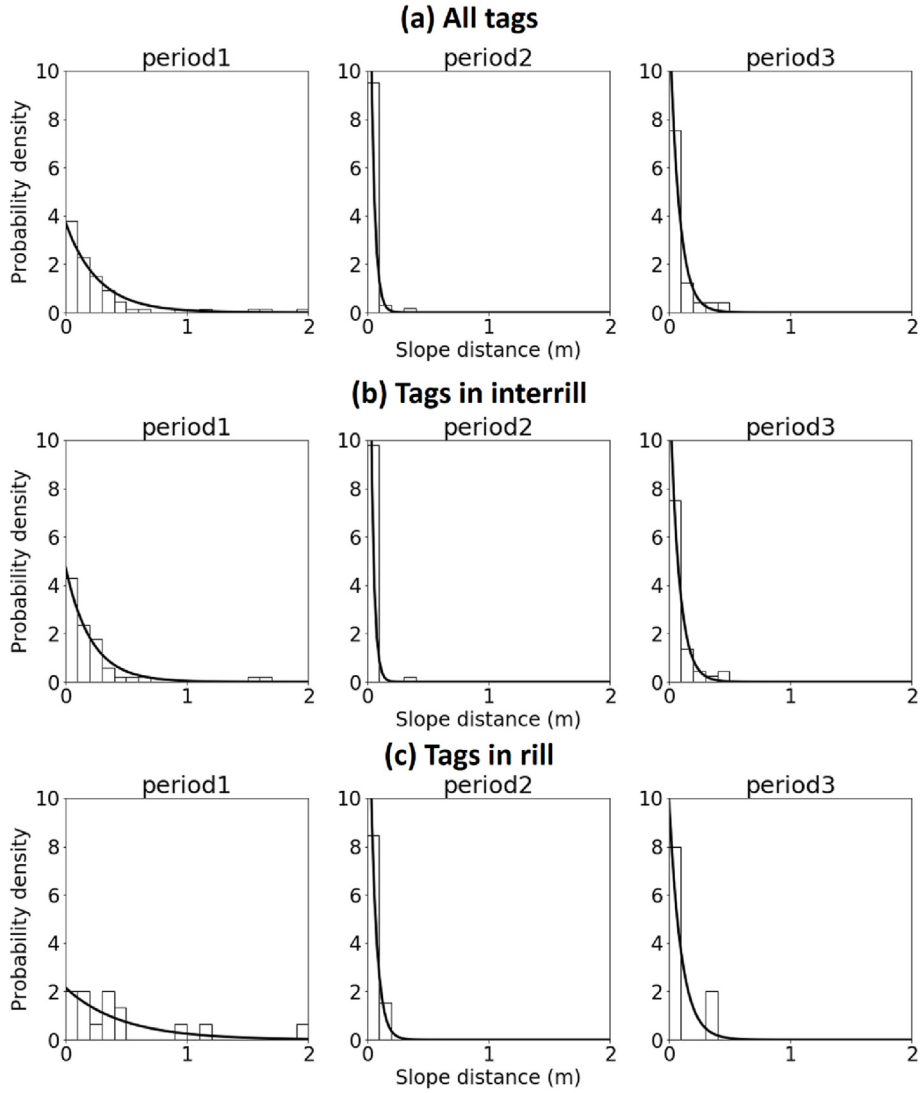

Fig. 9. Histogram of transport distance of RFID tags. Solid lines showed model of rain splashed transport distance by van Dijk et al. (2002) and Furbish et al. (2007).

Acknowledgments

This work was funded by the Ministry of Education, Culture, Sports and Science and the Nuclear Regulation Authority of Japan. This work was also supported by Grant-in-Aid for Scientific Research on Innovative Areas Grant Number 24110006.

References

Agisoft, 2017. PhotoScan User Manual Professional Edition.

Armstrong, A., Quinton, J.N., Maher, B.A., 2012. Thermal enhancement of natural magnetism as a tool for tracing eroded soil. Earth Surf. Process. Landf. 37, 1567–1572. https://doi.org/10.1002/esp.3312.

Bagarello, V., Ferro, V., Giordano, G., Mannocchi, F., Todisco, F., Vergni, L., 2018. Statistical check of USLE-M and USLE-MM to predict bare plot soil loss in two Italian environments. Land Degrad. Dev. 29 (8), 2614–2628. https://doi.org/10.1002/ldr.3072.

Barneveld, R.J., Seeger, M., Maalen-Johansen, I., 2013. Assessment of terrestrial laser scanning technology for obtaining high-resolution DEMs of soils. Earth Surf. Process. Landf. 38, 90–94. https://doi.org/10.1002/esp.3344.

Beck, H.E., Zimmermann, N.E., McVicar, T.R., Vergopolan, N., Berg, A., Wood, E.F., 2018. Present and future köppen-geiger climate classification maps at 1-km resolution. Scientific Data 5, 1–12. https://doi.org/10.1038/sdata.2018.214.

Beniaich, A., Silva, M.L.N., Guimarães, D.V., Avalos, F.A.P., Terra, F.S., Menezes, M.D., Avanzi, J.C., Cândido, B.M., 2022. UAV-based vegetation monitoring for assessing the impact of soil loss in olive orchards in Brazil. Geoderma Regional 30, e00543. https://doi.org/10.1016/j.geodrs.2022.e00543.

Borrelli, P., Alewell, C., Alvarez, P., Ayach Anache, J.A., Baartman, J., Ballabio, C., … Panagos, P., 2021. Soil erosion modelling: a global review and statistical analysis. Sci. Total Environ. 780, 146494. https://doi.org/10.1016/j.scitotenv.2021.146494.

Borselli, L., Cassi, P., Torri, D., 2008. Prolegomena to sediment and flow connectivity in the landscape: a GIS and field numerical assessment. Catena 75, 268–277. https://doi.org/10.1016/j.catena.2008.07.006.

Brown, L.C., Foster, G.R., 1987. Storm erosivity using idealized intensity distributions. Trans. ASAE 30, 0379–0386. https://doi.org/10.13031/2013.31957.

Cavalli, M., Trevisani, S., Comiti, F., Marchi, L., 2013. Geomorphometric assessment of spatial sediment connectivity in small alpine catchments. Geomorphology 188, 31–41. https://doi.org/10.1016/j.geomorph.2012.05.007.

Cerdà, A., Novara, A., Dlapa, P., López-Vicente, M., Úbeda, X., Popović, Z., Mekonnen, M., Terol, E., Janizadeh, S., Mbarki, S., Saldanha-Vogelmann, E., Hazrati, S., Sannigrahi, S., Parhizkar, M., Giménez-Morera, A., 2021. Rainfall and water yield in Macizo del Caroig, Eastern Iberian Peninsula. Event runoff at plot scale during a rare flash flood at the Barranco de Benacancil. Geogr. Res. Lett. (Cuadernos de Investigación Geográfica) 47 (1), 95–119. https://doi.org/10.18172/cig.4833.

Cerdan, O., Poesen, J., Govers, G., Saby, N., Le Bissonnais, Y., Gobin, A., Vacca, A., Quinton, J., Auerswald, K., Klik, A., Kwaad, F.F.P.M., Roxo, M.J., 2006. Chapter 38. Sheet and rill erosion. In: Boardman, John, Poesen, Jean (Eds.), Soil Erosion in Europe. Wiley, pp. 347–369. https://doi.org/10.1002/0470859202.ch38.

Cucchiaro, S., Fallu, D.J., Zhang, H., Walsh, K., Van Oost, K., Brown, A.G., Tarolli, P., 2020. Multiplatform-SfM and TLS data fusion for monitoring agricultural terraces in complex topographic and landcover conditions. Remote Sens. 12, 1946. https://doi.org/10.3390/rs12121946.

Darboux, F., Davy, P., Gascuel-Odoux, C., Huang, C., 2002. Evolution of soil surface roughness and flowpath connectivity in overland flow experiments. Catena 46, 125–139. https://doi.org/10.1016/S0341-8162(01)00162-X.

Ding, W., Huang, C., 2017. Effects of soil surface roughness on interrill erosion processes and sediment particle size distribution. Geomorphology 295, 801–810. https://doi.org/10.1016/j.geomorph.2017.08.033.

Ellison, W.D., 1947. Soil erosion studies - part I. Agric. Eng. 28, 145–146.

Eltner, A., Baumgart, P., Maas, H.G., Faust, D., 2015. Multi-temporal UAV data for automatic measurement of rill and interrill erosion on loess soil. Earth Surf. Process. Landf. 40, 741–755. https://doi.org/10.1002/esp.3673.

Eltner, A., Kaiser, A., Castillo, C., Rock, G., Neugirg, F., Abellán, A., 2016. Image-based surface reconstruction in geomorphometry-merits, limits and developments. Earth Surf. Dyn. 4, 359–389. https://doi.org/10.5194/esurf-4-359-2016.

Fernández-Raga, M., Palencia, C., Keesstra, S., Jordán, A., Fraile, R., Angulo-Martínez, M., Cerdà, A., 2017. Splash erosion: a review with unanswered questions. Earth Sci. Rev. 171, 463–477. https://doi.org/10.1016/j.earscirev.2017.06.009.

Furbish, D.J., Hammer, K.K., Schmeeckle, M., Borosund, M.N., Mudd, S.M., 2007. Rain splash of dry sand revealed by high-speed imaging and sticky paper splash targets. J. Geophys. Res. Earth Surf. 112, 1–19. https://doi.org/10.1029/2006JF000498.

Gabet, E.J., Dunne, T., 2003. Sediment detachment by rain power. Water Resour. Res. 39: ESG 1-1-ESG, 1–12. https://doi.org/10.1029/2001wr000656.

Ghahramani, A., Yoshiharu, I., Mudd, S.M., 2012. Field experiments constraining the probability distribution of particle travel distances during natural rainstorms on different slope gradients. Earth Surf. Process. Landf. 37, 473–485. https://doi.org/10.1002/esp.2253.

Gilley, J.E., 2005. EROSION | water-induced. Encyclopedia of Soils in the Environment (Editor-in-Chief: Daniel Hillel). Elsevier. ISBN: 978-0-12-348530-4, pp. 463–469. https://doi.org/10.1016/B0-12-348530-4/00262-9.

Glendell, M., McShane, G., Farrow, L., James, M.R., Quinton, J., Anderson, K., Evans, M., Benaud, P., Rawlins, B., Morgan, D., Jones, L., Kirkham, M., DeBell, L., Quine, T.A., Lark, M., Rickson, J., Brazier, R.E., 2017. Testing the utility of structure-from-motion photogrammetry reconstructions using small unmanned aerial vehicles and ground photography to estimate the extent of upland soil erosion. Earth Surf. Process. Landf. 42 (12), 1860–1871. https://doi.org/10.1002/esp.4142.

Gómez, J.A., Nearing, M.A., 2005. Runoff and sediment losses from rough and smooth soil surfaces in a laboratory experiment. Catena 59, 253–266. https://doi.org/10.1016/j.catena.2004.09.008.

Hairsine, P.B., Rose, C.W., 1991. Rainfall detachment and deposition: sediment transport in the absence of flow-driven processes. Soil Sci. Soc. Am. J. 55, 320. https://doi.org/10.2136/sssaj1991.03615995005500020003x.

Hooke, J., Souza, J., 2021. Challenges of mapping, modelling and quantifying sediment connectivity. Earth Sci. Rev. 223, 103847. https://doi.org/10.1016/j.earscirev.2021.103847.

Igarashi, Y., Onda, Y., Wakiyama, Y., Yoshimura, K., Kato, H., Kozuka, S., Manome, R., 2021. Impacts of freeze-thaw processes and subsequent runoff on ^{137}Cs washoff from bare land in Fukushima. Sci. Total Environ. 769, 144706. https://doi.org/10.1016/j.scitotenv.2020.144706.

Kaiser, A., Erhardt, A., Eltner, A., 2018. Addressing uncertainties in interpreting soil surface changes by multitemporal high-resolution topography data across scales. Land Degrad. Dev. 29, 2264–2277. https://doi.org/10.1002/ldr.2967.

Kayad, A., Rainato, R., Picco, L., Sartori, L., Marinello, F., 2019. Assessing topsoil movement in rotary harrowing process by RFID (radio-frequency identification) technique. Agriculture 9 (8), 184. https://doi.org/10.3390/agriculture9080184.

Keesstra, S., Nunes, J.P., Saco, P., Parsons, T., Poeppl, R., Masselink, R., Cerdà, A., 2018. The way forward: can connectivity be useful to design better measuring and modelling schemes for water and sediment dynamics? Sci. Total Environ. 644, 1557–1572. https://doi.org/10.1016/j.scitotenv.2018.06.342.

Keesstra, S.D., Bagarello, V., Ferro, V., Finger, D., Parsons, A.J., 2020. Connectivity in hydrology and sediment dynamics. Land Degrad. Dev. 31, 2525–2528. https://doi.org/10.1002/ldr.3401.

Laceby, J.P., Chartin, C., Evrard, O., Onda, Y., Garcia-Sanchez, L., Cerdan, O., 2016. Rainfall erosivity in catchments contaminated with fallout from the Fukushima Daiichi nuclear power plant accident. Hydrol. Earth Syst. Sci. 20, 2467–2482. https://doi.org/10.5194/hess-20-2467-2016.

Lamarre, H., MacVicar, B., Roy, A.G., 2005. Using passive integrated transponder (PIT) tags to investigate sediment transport in gravel-bed Rivers. J. Sediment. Res. 75, 736–741. https://doi.org/10.2110/jsr.2005.059.

Liang, X., Feng, J., Ye, Z., Zhang, L., Li, J., Lu, X., Zhao, S., Liu, Q., Zheng, Z., Wang, Y., 2023. The effect of soil surface mounds and depressions on runoff. Sustainability 15 (1), 175. https://doi.org/10.3390/su15010175.

Long, E.J., Hargrave, G.K., Cooper, J.R., Kitchener, B.G.B., Parsons, A.J., Hewett, C.J.M., Wainwright, J., 2014. Experimental investigation into the impact of a liquid droplet onto a granular bed using three-dimensional, time-resolved, particle tracking. Phys. Rev. E Stat. Nonlinear Soft Matter Phys. 89, 1–14. https://doi.org/10.1103/PhysRevE.89.032201.

López-Vicente, M., Guzmán, G., 2021. Measuring soil erosion and sediment connectivity at distinct scales (Book Chapter). Precipitation: Earth Surface Responses and Processes, pp. 287–326. https://doi.org/10.1016/B978-0-12-822699-5.00011-2.

López-Vicente, M., Sun, X., Onda, Y., Kato, H., Gomi, T., Hiraoka, M., 2017. Effect of tree thinning and skidding trails on hydrological connectivity in two Japanese forest catchments. Geomorphology 292, 104–114. https://doi.org/10.1016/j.geomorph.2017.05.006.

López-Vicente, M., Cerdà, A., Kramer, H., Keesstra, S., 2021. Post-fire practices benefits on vegetation recovery and soil conservation in a Mediterranean area. Land Use Policy 111, 105776. https://doi.org/10.1016/j.landusepol.2021.105776.

Lu, X., Li, Y., Washington-Allen, R.A., Li, Y., 2019. Structural and sedimentological connectivity on a rilled hillslope. Sci. Total Environ. 655, 1479–1494. https://doi.org/10.1016/j.scitotenv.2018.11.137.

Lucieer, A., de Jong, S.M., Turner, D., 2014. Mapping landslide displacements using structure from motion (SfM) and image correlation of multi-temporal UAV photography. Prog. Phys. Geogr. 38, 97–116. https://doi.org/10.1177/0309133313515293.

Martini, L., Cavalli, M., Picco, L., 2022. Predicting sediment connectivity in a mountain basin: a quantitative analysis of the index of connectivity. Earth Surf. Process. Landf. 47 (6), 1500–1513. https://doi.org/10.1002/esp.5331.

Moreno-De Las Heras, M., Nicolau, J.M., Merino-Martn, L., Wilcox, B.P., 2010. Plot-scale effects on runoff and erosion along a slope degradation gradient. Water Resour. Res. 46, 1–12. https://doi.org/10.1029/2009WR007875.

Ni, S., Wen, H., Wilson, G.V., Cai, C., Wang, J., 2022. A simulated study of surface morphological evolution on coarse-textured soils under intermittent rainfall events. Catena 208, 105767. https://doi.org/10.1016/j.catena.2021.105767.

Nichols, M.H., 2004. A radio frequency identification system for monitoring coarse sediment particle displacement. Appl. Eng. Agric. 20, 783–787.

Onda, Y., Taniguchi, K., Yoshimura, K., Kato, H., Takahashi, J., Wakiyama, Y., Coppin, F., Smith, H., 2020. Radionuclides from the Fukushima Daiichi nuclear power plant in terrestrial systems. Nat. Rev. Earth Environ. 1, 644–660. https://doi.org/10.1038/s43017-020-0099-x.

Pagán, J.I., Bañón, L., López, I., Bañón, C., Aragonés, L., 2019. Monitoring the dune-beach system of Guardamar del Segura (Spain) using UAV, SfM and GIS techniques. Sci. Total Environ. 687, 1034–1045. https://doi.org/10.1016/j.scitotenv.2019.06.186.

Parsons, A.J., Wainwright, J., Powell, D.M., Kaduk, J., Brazier, R.E., 2004. A conceptual model for determining soil erosion by water. Earth Surf. Process. Landf. 29, 1293–1302. https://doi.org/10.1002/esp.1096.

Parsons, A.J., Brazier, R.E., Wainwright, J., Powell, D.M., 2006. Scale relationships in hillslope runoff and erosion. Earth Surf. Process. Landf. 31, 1384–1393. https://doi.org/10.1002/esp.1345.

Parsons, A.J., Wainwright, J., Fukuwara, T., Onda, Y., 2010. Using sediment travel distance to estimate medium-term erosion rates: a 16-year record. Earth Surf. Process. Landf. 35, 1694–1700. https://doi.org/10.1002/esp.2011.

Parsons, A.J., Onda, Y., Noguchi, T., Patin, J., Cooper, J., Wainwright, J., Sakai, N., 2014. The use of RFID in soil-erosion research. Earth Surf. Process. Landf. 39, 1693–1696. https://doi.org/10.1002/esp.3628.

Parsons, A.J., Bracken, L., Poeppl, R.E., Wainwright, J., Keesstra, S.D., 2015. Introduction to special issue on connectivity in water and sediment dynamics. Earth Surf. Process. Landf. 40, 1275–1277. https://doi.org/10.1002/esp.3714.

Parsons, A., Cooper, J., Onda, Y., Sakai, N., 2018. Application of RFID to soil-erosion research. Applied Sciences (Switzerland) 8, 1–11. https://doi.org/10.3390/app8122511.

Renard, K.G., Foster, G.R., Weesies, G.A., McCool, D.K., Yoder, D.C., 1997. Predicting soil erosion by water: a guide to conservation planning with the revised universal soil loss equation (RUSLE). Agriculture Handbook No. 703. Agriculture Handbook, p. 49.

Ritchie, J.C., 2000. Soil erosion. In: Schultz, G.A., Engman, E.T. (Eds.), Remote Sensing in Hydrology and Water Management. Springer, Berlin, Heidelberg https://doi.org/10.1007/978-3-642-59583-7_12 Online ISBN: 978-3-642-59583-7.

Roth, D.L., Doane, T.H., Roering, J.J., Furbish, D.J., Zettler-Mann, A., 2020. Particle motion on burned and vegetated hillslopes. Proc. Natl. Acad. Sci. U. S. A. 117, 25335–25343. https://doi.org/10.1073/pnas.1922495117.

Sartori, M., Philippidis, G., Ferrari, E., Borrelli, P., Lugato, E., Montanarella, L., Panagos, P., 2019. A linkage between the biophysical and the economic: assessing the global market impacts of soil erosion. Land Use Policy 86, 299–312. https://doi.org/10.1016/j.landusepol.2019.05.014.

Savat, J., Poesen, J., 1981. Detachment and transportation of loose sediments by raindrop splash. Catena 8, 1–17. https://doi.org/10.1016/S0341-8162(81)80001-X.

Stöcker, C., Eltner, A., Karrasch, P., 2015. Measuring gullies by synergetic application of UAV and close range photogrammetry - a case study from Andalusia, Spain. Catena 132, 1–11. https://doi.org/10.1016/j.catena.2015.04.004.

Takahara, S., Ikegami, M., Yoneda, M., Kondo, H., Ishizaki, A., Iijima, M., Shimada, Y., Matsui, Y., 2017. Bioaccessibility of Fukushima-accident-derived Cs in soils and the contribution of soil ingestion to radiation doses in children. Risk Anal. 37 (7), 1256–1267. https://doi.org/10.1111/risa.12694.

Thomsen, L.M., Baartman, J.E.M., Barneveld, R.J., Starkloff, T., Stolte, J., 2015. Soil surface roughness: comparing old and new measuring methods and application in a soil erosion model. Soil 1, 399–410. https://doi.org/10.5194/soil-1-399-2015.

Tonkin, T.N., Midgley, N.G., Graham, D.J., Labadz, J.C., 2014. The potential of small unmanned aircraft systems and structure-from-motion for topographic surveys: a test of emerging integrated approaches at Cwm Idwal, North Wales. Geomorphology 226, 35–43. https://doi.org/10.1016/j.geomorph.2014.07.021.

Torri, D., Sfalanga, M., Del Sette, M., 1987. Splash detachment: runoff depth and soil cohesion. Catena 14, 149–155. https://doi.org/10.1016/S0341-8162(87)80013-9.

Trevisani, S., Cavalli, M., 2016. Topography-based flow-directional roughness: potential and challenges. Earth Surf. Dyn. 4, 343–358. https://doi.org/10.5194/esurf-4-343-2016.

van Dijk, A.I.J.M., Meesters, A.G.C.A., Bruijnzeel, L.A., 2002. Exponential distribution theory and the interpretation of splash detachment and transport experiments. Soil Sci. Soc. Am. J. 66, 1466–1474. https://doi.org/10.2136/sssaj2002.1466.

Wainwright, J., Parsons, A.J., Müller, E.N., Brazier, R.E., Powell, D.M., Fenti, B., 2008. A transport-distance approach to scaling erosion rates: 1. Background and model development. Earth Surf. Process. Landf. 33, 813–826. https://doi.org/10.1002/esp.1624.

Wainwright, J., Turnbull, L., Ibrahim, T.G., Lexartza-Artza, I., Thornton, S.F., Brazier, R.E., 2011. Linking environmental régimes, space and time: interpretations of structural and functional connectivity. Geomorphology 126, 387–404. https://doi.org/10.1016/j.geomorph.2010.07.027.

Wang, R., Li, P., Li, Z., Yu, K., Han, J., Zhu, Y., Su, Y., 2021. Effects of gully head height and soil texture on gully headcut erosion in the Loess Plateau of China. Catena 207, 105674. https://doi.org/10.1016/j.catena.2021.105674.

Wilcox, B.P., Breshears, D.D., Allen, G.D., 2003. Ecohydrology of a resource-conserving semi-arid woodland: effects of scale and disturbance. Ecol. Monogr. 73, 223–239.

Wischmeier, W.H., Smith, D.D., 1978. Predicting rainfall erosion losses. Agric. Handb. 537, 285–291. https://doi.org/10.1029/TR039i002p00285.

Yoshimura, K., Onda, Y., Kato, H., 2015. Evaluation of radiocaesium wash-off by soil erosion from various land uses using USLE plots. J. Environ. Radioact. 139, 362–369. https://doi.org/10.1016/j.jenvrad.2014.07.019.